



**Low Temperature Structures and Magnetic Interactions in
the Organic-based Ferromagnetic and Metamagnetic
Polymorphs of Decamethylferrocenium 7,7,8,8-Tetracyano-
p-quinodimethanide, [FeCp*₂]⁺[TCNQ]⁻**

Journal:	<i>Dalton Transactions</i>
Manuscript ID	DT-ART-06-2021-002106.R1
Article Type:	Paper
Date Submitted by the Author:	21-Jul-2021
Complete List of Authors:	Miller, Joel; University of Utah, Department of Chemistry Dasilva, Jack; University of Utah, Department of Chemistry Fumanal, Maria; University of Barcelona, Department of Physical Chemistry Lapidus, Saul; Argonne National Laboratory X-Ray Sciences Division, Advanced Photon Source; Argonne National Lab Novoa, Juan; University of Barcelona, Department of Physical Chemistry Rheingold, Arnold; University of California, Department of Chemistry and Biochemistry Ribas-Ariño, Jordi; Universitat de Barcelona, Departament de Química Física Stephens, Peter; Stony Brook University

Low Temperature Structures and Magnetic Interactions in the Organic-based Ferromagnetic and Metamagnetic Polymorphs of Decamethylferrocenium 7,7,8,8-Tetracyano-*p*-quinodimethanide, [FeCp*₂]⁺[TCNQ]⁻

Saul H. Lapidus,^{†¶} Peter W. Stephens,^{†*} Maria Fumanal,[#] Jordi Ribas-Ariño,[#] Juan J. Novoa,^{*#} Jack G. DaSilva,[§] Arnold L. Rheingold,[‡] Joel S. Miller^{§*}

Department of Physics & Astronomy, Stony Brook University, Stony Brook, New York 11794-3800 USA

Department of Materials Chemistry and Physical Chemistry and IQTCUB, University of Barcelona, Av. Diagonal, 645, E-08028, Barcelona, Spain

Department of Chemistry and Biochemistry, University of California, San Diego, La Jolla, California 92093-0358 USA

Department of Chemistry, University of Utah, 315 S. 1400 E. RM 2020, Salt Lake City, UT 84112-0850 USA

Dedicated to the memory of Professor Joel Bernstein (1941-2019), a pioneer of polymorphic materials, and also to Dedicated to Professors Jaume Veciana and Concepció Rovira for their sustained contributions for the development of molecule-based electronics and magnetism

Abstract

To identify the genesis of the differing magnetic behaviors for the ferro- (**FO**) and metamagnetic (**MM**) polymorphs of $[\text{FeCp}^*_2][\text{TCNQ}]$ (Cp^* = pentamethylcyclopentadienide; TCNQ = 7,7,8,8-tetracyano-*p*-quinodimethane) the low temperature (18 ± 1 K) structures of each polymorph were determined from high-resolution synchrotron powder diffraction data. Each polymorph possesses chains of alternating $S = 1/2$ $[\text{FeCp}^*_2]^{++}$ cations and $S = 1/2$ $[\text{TCNQ}]^{+}$, but with differing relative orientations. These as well as an additional paramagnetic polymorph do not thermally interconvert. In addition, the room and low ($<70 \pm 10$ K) temperature structures of the **MM** polymorph, **MM_{RT}** and **MM_{LT}**, respectively, differ from that previously reported at 167 K (-106 °C) **MM** structure, and no evidence of either phase transition was previously noted even from the magnetic data. This transition temperature and enthalpy of this phase transition for **MM_{RT}** \rightleftharpoons **MM** was determined to be 226.5 ± 0.4 K (-46.7 ± 0.4 °C) and 0.68 ± 0.04 kJ/mol upon warming, respectively, from differential calorimetry studies (DSC). All three **MM** phases are triclinic ($P\bar{1}$) with the room temperature phase having a doubled unit cell relative to the other two. The lower temperature phase transition involves a small rearrangement of the molecular ions and shift in lattice parameters. These three **MM** and **FO** polymorphs have been characterized and form extended 1-D chains with alternating $S = 1/2$ $[\text{FeCp}^*_2]^{++}$ cations, and $S = 1/2$ $[\text{TCNQ}]^-$ anions, whereas the fifth, paramagnetic (**P**) polymorph possesses $S = 0$ π - $[\text{TCNQ}]_2^{2-}$ dimers. At 18 ± 1 K the intrachain Fe•••Fe separations are 10.738(2) and 10.439(3) Å for the **FO** and **MM_{LT}** polymorphs, respectively. The key structural differences between **FO** and **MM_{LT}** at 18 ± 1 K are the 10% shorter interchain N•••N and the 2.8% shorter intrachain Fe•••Fe separation present for **MM_{LT}**. Computational analysis of all nearest-neighbor spin couplings for the 18-K structures of **FO** and **MM_{LT}** indicates that the intrachain $[\text{FeCp}^*_2]^{++}\bullet\bullet\bullet[\text{TCNQ}]^-$ spin couplings ($H = -2S_i\bullet S_j$) are the strongest (4.95 and 6.5 cm^{-1} for **FO** and **MM_{LT}**, respectively), as previously hypothesized, and are ferromagnetic due to their $S = 1/2$ spins residing in orthogonal orbitals. The change in relative $[\text{TCNQ}]^- \bullet\bullet\bullet [\text{TCNQ}]^-$ orientations leads to a computed change from the ferromagnetic interaction (0.2 cm^{-1}) for **FO** to an antiferromagnetic interaction (-0.1 cm^{-1}) for **MM_{LT}** in accord with its observed antiferromagnetic ground state. Hence, the magnetic ground state cannot be solely described by the dominant magnetic interactions.

Introduction

Organic-based materials possessing bulk, cooperative physical properties are a contemporary research area that spans chemistry, materials science, and physics.¹ Examples of organic-based magnets,² superconductors,³ and ferroelectrics⁴ have been established. These materials have the common feature of having delocalized π -electrons that are essential for the physical property. $[\text{Fe}^{\text{III}}\text{Cp}^*_2]^+[\text{TCNQ}]^-$ (TCNQ = 7,7,8,8-tetracyano-*p*-quinodimethane; Cp^* = pentamethylcyclopentadienide, C_5Me_5^-) was reported to order as a metamagnet below 2.55 K,^{5,6,7} and by substitution of TCNQ with TCNE (tetracyanoethylene) led to the discovery of the first organic-based ferromagnet, $[\text{Fe}^{\text{III}}\text{Cp}^*_2]^+[\text{TCNE}]^-$,^{8,9} which has a similar structural motif,^{10,11} but magnetically orders as a bulk ferromagnet with a magnetic ordering temperature (T_c) of 4.8 K.^{12,13}

$[\text{FeCp}^*_2][\text{TCNQ}]$ has been reported to form three different magnetic polymorphs, namely, a dimeric paramagnet (**P**),^{6,14} a ferromagnet (**FO**) ($T_c = 3.1$ K),^{7,15} and the aforementioned metamagnet (**MM**).^{6,7} The **FO** and **MM** polymorphs possess parallel $\cdots\text{D}^+\text{A}^-\text{D}^+\text{A}^- \cdots$ 1-D chains ($\text{D} = \text{FeCp}^*_2$; $\text{A} = \text{TCNQ}$), which is similar to that reported for the ferromagnet $[\text{FeCp}^*_2][\text{TCNE}]$.^{10,11,16} Based upon their respective reported room temperature and 167 K (-106 °C) structures, only a few key structural differences exist, but these are sufficient to render the significantly different properties observed for differing polymorphs.^{17,18}

Note that the structure of the **P** polymorph^{6,14} along with the metamagnetic properties of **MM**⁵ were reported first. The structure of **MM** was subsequently reported,⁶ however, in a preliminary communication,¹⁶ the structure of the then-unknown **FO** polymorph was described.¹⁵

The previous structural determinations of $[\text{FeCp}^*_2][\text{TCNQ}]$ were performed significantly above T_c , where the cation C_5Me_5 (Cp^*) rings are in an eclipsed conformation (D_{5h}) for **FO**, but staggered (D_5) for **MM**. Additionally, the interchain arrangements have some small, but notable differences: the $[\text{TCNQ}]^-$ anions in adjacent layers of **MM** in are arranged in the same direction, but zigzag for **FO**.¹⁵ Thus, the closest $\text{N}\cdots\text{N}$ $[\text{TCNQ}]^- \cdots [\text{TCNQ}]^-$ distance in **MM** is 4.080 Å vs. 4.337 Å for **FO**, albeit at different temperatures. Due to the closer distance in **MM** than in **FO**, the expectation that this interaction should lead to stronger antiferromagnetic coupling, and the antiferromagnetic ground state is expected for this configuration.^{7,12,19} Above the 1300 Oe critical field the **MM** polymorph switches to a ferromagnetic-like state.⁷ To understand the magnetic couplings, however, requires the knowledge of the structures at temperatures as close as feasible to where the magnetic ordering is observed.

To understand the subtle structural differences between the **FO** and **MM** polymorphs and how they affect the magnetic properties of this unique system, where different polymorphs have ferro- and antiferromagnetic ground states, very low temperature structures are herein reported (although still above than the magnetic ordering temperatures) for both phases. These form the basis for theoretical evaluations of the magnetic interactions with a very high degree of accuracy, aiming at providing benchmark results that will provide a solid foundation for the analysis and rationalization of the subtle spin coupling interactions that lead to the different magnetic ground states.²⁰ In addition, although there is no evidence from the magnetic data, two reversible structural phase transitions **MM** phase were discovered; both at higher ($\mathbf{MM} \rightleftharpoons \mathbf{MM}_{\text{RT}}$) and at low temperature ($\mathbf{MM} \rightleftharpoons \mathbf{MM}_{\text{LT}}$) that have not been previously published.

Experimental Section

The purple-reflecting crystals of the **MM** and **FO** polymorphs were prepared as previously reported.⁷ Differential scanning calorimetry (DSC) studies utilized a TA Instruments Model 2910 DSC equipped with a LNCA liquid nitrogen cooling accessory enabling operation between of -150 to 550 °C using a 1 °C/min scan rate and ~5 mg samples. Consecutive heating and cooling cycles were performed to ensure reversibility and reproducibility of the phase transitions. Computational results were obtained as previously reported.¹⁰

High resolution powder diffraction measurements for the Rietveld structure analysis for the **MM** and **FO** polymorphs at various temperatures were performed at Beam Line X16C of the National Synchrotron Light Source at Brookhaven National Laboratory. The powdered samples were held in 1.0 mm diameter thin-wall quartz capillaries. X-Rays of a single wavelength were selected by a Si(111) channel cut crystal. Diffracted X-rays were selected by a Ge(111) analyzer and detected by a NaI scintillation counter. Samples were cooled either by an Oxford Cryostream ($T \geq 100$ K) or an APD closed cycle refrigerator ($T < 100$ K). To improve particle statistics, the sample was spun in the former case, and rocked in the latter, during data collection. The incident intensity was monitored by an ion chamber and used to normalize the measured signal. The TOPAS-Academic program was used to index, solve, and refine the crystal structures.^{21,22,23} Rietveld plots are given in Figures S1 - S3.

The single crystal structures of **MM** were determined on a Nonius KappaCCD diffractometer equipped with Mo K α radiation. All the reflections were merged and only those for

which $I_o > 2\sigma(I)$ were included in the refinement, where $\sigma(F_o)^2$ is the standard deviation based on counting statistics. The data were integrated using the Bruker SAINT software program.²⁴ The structures were solved by a combination of direct methods and heavy atom methods. Direct methods and the refinement by full-matrix least-squares methods using SHELXL-97 were used for the structures of **MM** at several temperatures. All the non-hydrogen atoms were refined with anisotropic displacement coefficients. Hydrogen atoms were assigned isotropic displacements $U(H) = 1.2U(C)$, and their coordinates were allowed to ride on their respective carbons using SHELXL97.²⁵

Results and Discussion

A fundamental understanding as the genesis of the magnetic couplings for the **FO** and for the **MM** polymorphs of $[\text{FeCp}^*_2][\text{TCNQ}]$ that lead to their observed ferro- and antiferromagnetic ordering and their subtle differences has yet to be identified. Insight into this system will provide a salient understanding of the couplings and competition among couplings that led to net antiferromagnetic as well as ferromagnetic couplings and subsequently long range, bulk magnetic ordering. A computational study of the magnetic couplings requires the structure determination preferably at or below the ordering temperature. The structures of the **MM** and **FO** polymorphs $[\text{FeCp}^*_2][\text{TCNQ}]$ have been reported at 167 K and at room temperature, respectively, but herein they are redetermined via high-resolution powder X-ray diffraction (PXRD) data at 18 ± 1 K. As part of these studies the room temperature structures were also obtained. The unit cell of the **FO** phase at room temperature is in accord with that previously reported,¹⁵ Table 1.

In contrast, the unit cell at room temperature for the **MM** is doubled from that previously reported at 167 K, Table 1, suggesting a phase transition between 167 K and room temperature. Lattice parameter measurements upon cooling show the room temperature phase persisting to 215 K. Single crystal measurements at 230, 265, and 300 K, Table 1, confirm the structure of the doubled cell of **MM** and provide a significantly more precise view of the molecular geometry in the room temperature phase. To further understand this phase transition differential scanning calorimetry (DSC) data was obtained and evaluated for **MM** (vide infra). Studies of the related MnCp^*_2 ²⁶ and $[\text{FeCp}^*_2][\text{TCNE}]$ ^{10,27} revealed structural transitions at similar temperatures. The prior 165 K structure of **MM** has an inversion center on the Fe atom, which implies that the Cp* rings have a staggered configuration. The transition in $[\text{FeCp}^*_2][\text{TCNE}]$ is from a staggered phase

to a disordered phase, whereas that in MnCp^*_2 is a rotation of the Cp^* rings, which is therefore more similar to that observed for **MM**.

In addition, a rearrangement of the structure was observed between 60 and 80 K, emphasizing the importance of using data collected at or near the magnetic ordering temperature to interpret magnetic interactions in molecular solids. The evolution of the temperature dependence of the lattice parameters of the **MM** phase is shown in Figure 1. Selected powder diffraction patterns, including two-phase coexistence at both transitions are shown in Figure S4. The phase transitions are clearly noted from the abrupt change in several unit cell parameters, *e.g.* b , c , α , β , and γ , over the entire temperature range, but the molar volume evolves continuously, Figure 1.

While the basic structure of the three **MM** phases consist of columns of alternating $[\text{FeCp}^*_2]^+$ and $[\text{TCNQ}]^-$ radical ions in roughly a triangular arrangement, *e.g.* Figure S7, but there are significant differences in their local arrangements. Figure 2 compares the environments of the **FO** and the three **MM** phases about one fixed TCNQ, showing the extent of the rearrangements among them. These structures are described in more detail below.

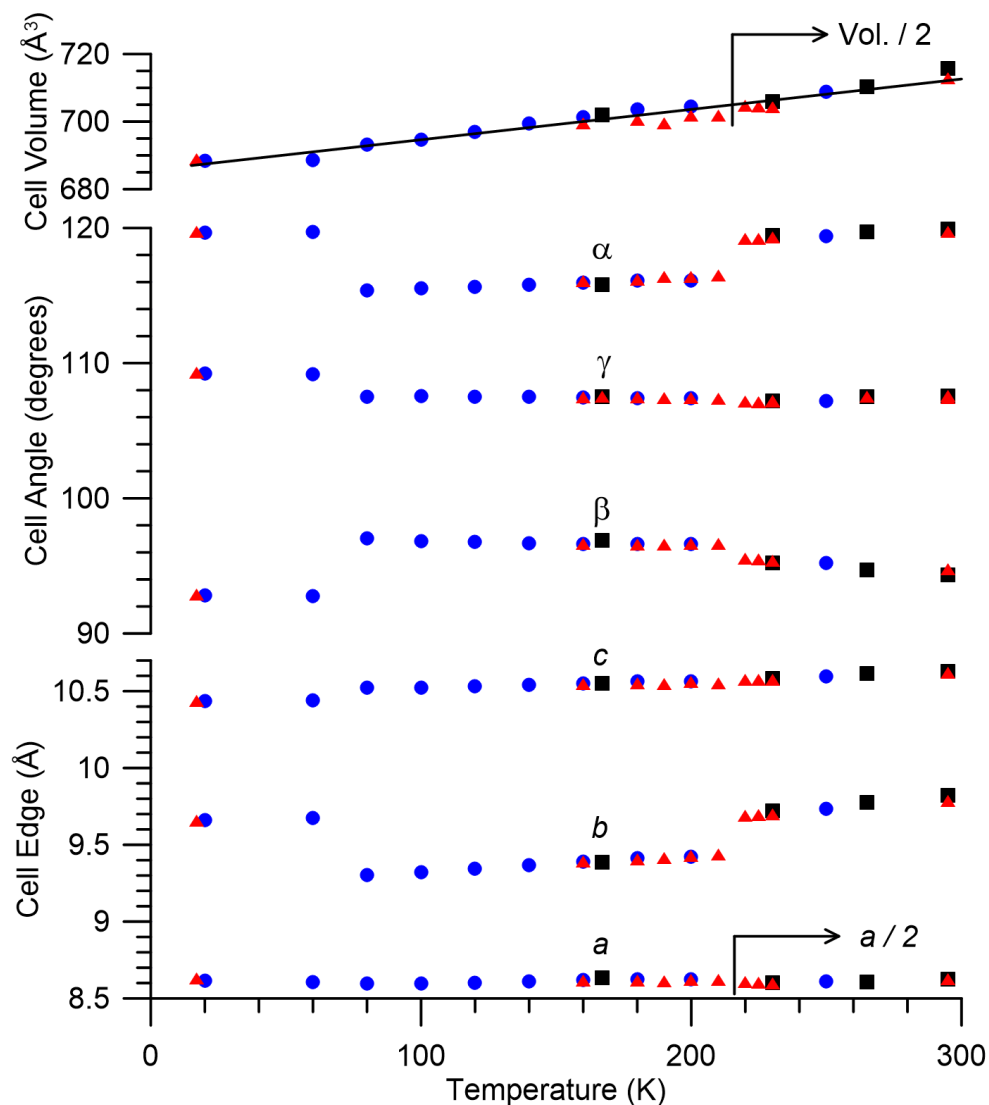


Figure 1. Unit cell lattice parameters of MM (MM_{LT} , MM , and MM_{RT}) as a function of temperature through the two structural transitions. Blue circles and red triangles are different powder samples; black squares are results from single crystal measurements. Values plotted outside of the 80 to 215 K range are not the reduced (Breuger) cell with three shortest non-coplanar translation vectors but are those that most closely match the shape of the intermediate temperature cell.

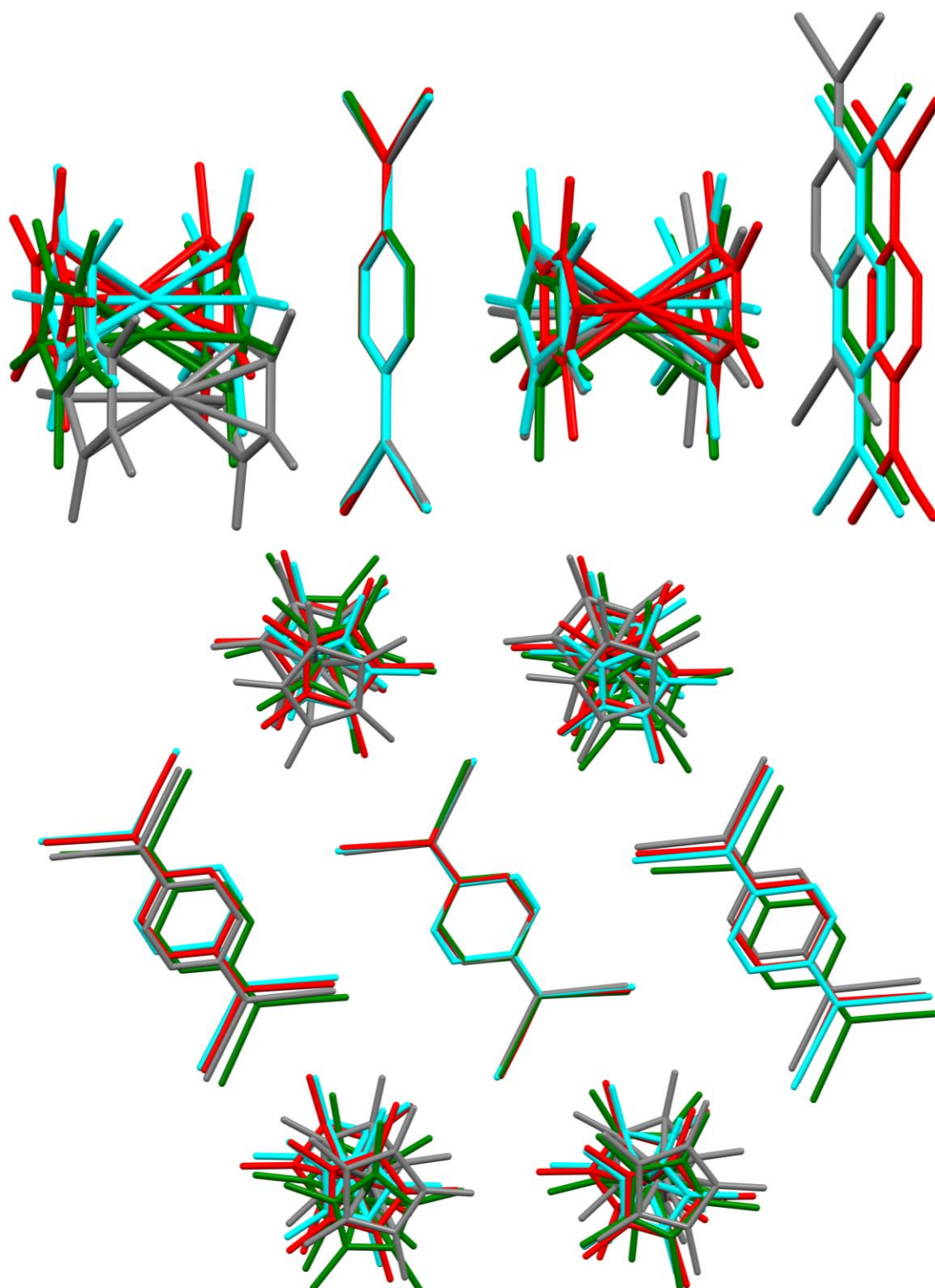


Figure 2. Overlay of the structures of the three **MM** and the **FO** phases, referenced to one TCNQ. Top: along the chain direction; bottom: plane perpendicular to the chain direction. Red: **MM** (167 K, MCFETC02); green: **MM_{RT}** (300 K, this work); cyan: **MM_{LT}** (17 K, this work); grey: **FO** (19 K, this work).

Table 1. Summary of the unit cell parameters for the **P**, **MM**, and **FO** polymorphs of [FeCp*₂][TCNQ].

	P	MM_{RT}	MM_{RT}	MM_{RT}	MM_{RT}	MM	MM_{LT}	FO	FO	FO	FO
<i>T</i> , K	RT ^a	300	RT ^a	265	230	167	17	RT ^a	RT ^a	RT	19
<i>a</i> , Å	9.708(1)	9.8228(12)	9.78875(13)	9.776(7)	9.7208(6)	8.635(4)	8.6314(3)	10.840(5)	10.837(2)	10.8717(6)	10.738(2)
<i>b</i> , Å	12.211(2)	10.2621(14)	10.2747(8)	10.268(8)	10.2659(6)	9.384(6)	9.6561(3)	30.999 (13)	31.356(7)	31.279(2)	30.815(6)
<i>c</i> , Å	23.585(4)	16.5194(19)	16.4859(2)	16.445(11)	16.4143(10)	10.635(9)	10.1192(3)	8.628(3)	8.609(1)	8.6165(6)	8.535(2)
α , °	90	103.762(3)	103.592(15)	103.63(2)	103.545(2)	116.76(5)	63.6721(7)	90	90	90	90
β , °	95.05(1)	92.367(4)	92.2522(8)	92.35(3)	91.978(2)	112.58(5)	68.4484(3)	99.20(3)	103.09(2)	102.325(9)	103.25(2)
γ , °	90	116.138(3)	116.102(1)	116.09(2)	116.119(2)	72.49(4)	70.721(4)	90	90	90	90
<i>V</i> , Å ³	2787.1(7)	1431.15(3)	1427.81(4)	1421(3)	1411.96(15)	701.8	688.77(6)	2862.96	2849.2(10)	2862.6(16)	2749.0(10)
<i>Z</i>	4	2	2	2	2	1	1	4	4	4	4
<i>Z'</i>	1	1	1	1	1	½	½	1	1	1	1
<i>V/Z</i> , Å ³	698.7	715.57	715.65	710.5	705.98	701.8	688.63	715.5	712.3	715.6	687.1
ρ , g/cm ³ (calc)	1.265	1.231	1.231	1.240	1.248	1.255	1.279	1.231	1.236	1.230	1.282
Fe ^{··} -Fe, ° Å	13.993	10.629	10.633	10.616	10.584	10.549	10.439	10.840	10.837	10.8717	10.738
Space group	<i>P</i> 2 ₁ / <i>c</i>	<i>P</i> 1̄	<i>P</i> 2 ₁ / <i>n</i>								
Method	SC ^b	SC ^b	PXRD ^c	SC ^{b,d}	SC ^b	SC ^b	PXRD ^c	SC ^b	SC ^b	PXRD ^{c,d}	PXRD ^c
[FeCp* ₂] ⁺ symmetry	~ <i>D</i> _{5h} ^f	<i>D</i> ₅	<i>D</i> ₅	<i>D</i> ₅	<i>D</i> ₅	<i>D</i> _{5d}	<i>D</i> _{5d}	~ <i>D</i> _{5h} ^f			
Ref	6, 14	This Work	This Work	This Work	This Work	6	This Work	16	15	This Work	This Work
CCDC Refcode/ Deposition	MCFETC01	2069829	2069080		MCFETC21	MCFETC02	2069078	MCFETC20	MCFETC03		2069079

^a Room temperature, 295 K ^b Single crystal ^c Powder X-ray diffraction ^d Unit cell only refined ^e Intrachain ^f Approximately, *D*_{5h}

The structures of the **FO** and three **MM** polymorphs of $[\text{FeCp}^*{}_{2}][\text{TCNQ}]$ at all temperatures are generally similar to that of $[\text{FeCp}^*{}_{2}][\text{TCNE}]$ ^{10,11} and possess parallel chains of alternating $[\text{FeCp}^*{}_{2}]^{+}$ cations, and $[\text{A}]^{-}$ ($\text{A} = \text{TCNQ}, \text{TCNE}$) anions. As for the **MM** and **FO** polymorphs the structure of the D_{2h} planar radical anionic $[\text{TCNQ}]^{-}$ are typical to those previously reported and are not discussed. Likewise, the structure of the $[\text{Fe}^{\text{III}}\text{Cp}^*{}_{2}]^{+}$ cations are those previously reported, and except for the relative orientation of the Cp^* rings, and are not discussed in detail. Each of these chains is surrounded by six parallel chains, two of which are in-registry (*i.e.* cations are near cations and anions are near anions in adjacent chains), and four of which are out-of-registry (*i.e.* cations are near anions in adjacent chains) (*vide infra*). The net magnetic coupling leading to magnetic ordering arises from the intra- and interchain couplings.

Structure of **FO**

The structure of the **FO** polymorph at 19 K is similar to that previously reported at room temperature,¹⁵ but with a 3.5% volume contraction, and the intrachain $\text{Fe}\cdots\text{Fe}$ separation decreases by 0.9% to 10.738 Å, Table 2. Each chain is surrounded by six parallel chains, Figure S5, forming two identical in-registry nearest neighbor chains, **I-II** and **I-II'** separated by 8.308 Å, as well as four out-of-registry nearest neighbor chains, **I-III**, **I-III'**, **I-IV** and **I-V** separated by 8.260, 8.260, 8.553, and 10.285 Å, respectively, Figure S6, Table 2. The shortest interchain $\text{Fe}\cdots\text{Fe}$, $\text{Fe}\cdots\text{N}$, and $\text{N}\cdots\text{N}$ separations are 8.535, 4.789, and 4.143 Å, respectively, Table 2. The $[\text{Fe}^{\text{III}}\text{Cp}^*{}_{2}]^{+}$ cation has a Fe-C distance of 2.147 Å, and $\text{Fe}\cdots\text{C}_5$ -ring centroid of 1.738 Å, with the two Cp^* rings being eclipsed, Figure 3a. Thus, the FeC_{10} core has approximate D_{5h} symmetry.

Table 2. Summary of key Fe•••Fe, Fe•••N, N•••N intra- and interchain bond distances and separations (Å) for the six nearest neighbor chains present for the **MM_{LT}** and **FO** polymorphs of [FeCp*₂][TCNQ] at 18 ± 1 K, and [FeCp*₂][TCNE] at 12 K.¹⁰

Compound	MM_{LT}	FO	[FeCp* ₂][TCNE]	Difference, Å, % (FO)-(MM _{LT}), (vs. FO)	Difference, Å, % (FO) - [FeCp* ₂][TCNE], (vs. FO)	Difference, Å, % (MM _{LT}) - [FeCp* ₂][TCNE], (vs. MM _{LT})
Temperature, T, K	17	19	12			
Fe•••Fe intrachain, Å	10.439	10.738	10.415	0.299, 2.78	0.323, 3.01	0.024, 0.23
in-registry N•••N interchain, Å	3.729 x2	4.143 x2	3.408 x2	0.414, 9.99	0.735, 17.8	0.321, 8.61
in-registry Fe•••Fe interchain, Å	8.631 x2 13.204 x2 13.878 x2	8.535 x2 12.089 x2 15.171 x2	8.205 x2 13.123 x2 13.758 x2	-0.085,-0.99	0.330, 3.87	0.426, 4.93
in-registry interchain separation, Å	8.620 x2	8.308 x2	8.182 x2	-0.312, -3.76	0.126, 1.52	0.438, 5.08
out-of-registry Fe•••N interchain, ^a Å	5.225 x2 5.336 5.855	4.789 4.973 x2/3 5.700 x2/3 5.709 x1/2 5.718 x1/2 5.820 x2/3	5.042 5.311 5.563 5.594 6.157 6.984 7.185	-0.436, 9.10	-0.253, -5.28	0.183, 3.50
out-of-registry Fe•••Fe interchain, Å	9.656 10.119 10.616 10.618	9.355 x2 10.020 10.179 10.417 x2 10.884 12.540	9.087 x2 9.318 x2 9.422 x2 9.664 x2 17.414 x2 17.272 x2	-0.301, 3.22	0.268, 2.86	0.569, 5.89
out-of-registry interchain separation, Å	8.389 x2 9.245 x2	8.260 x2 8.553 10.285	7.359 x2 7.918 x2	-0.129, -1.56	0.901, 10.9	1.030, 12.3

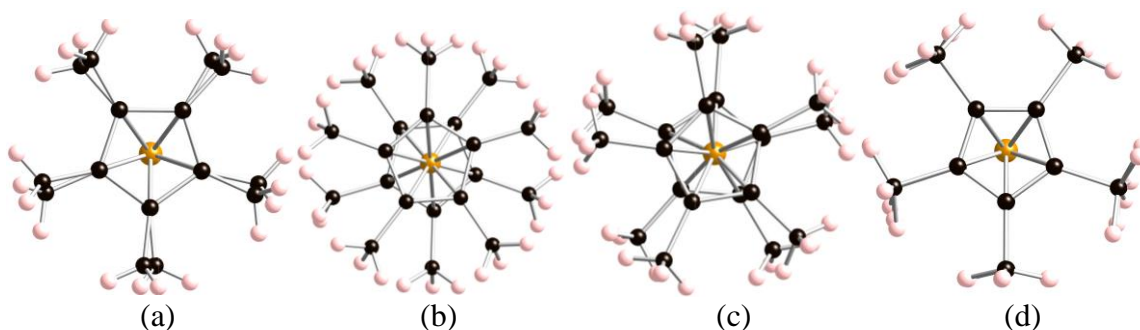


Figure 3. Top view along the C_5 axis of [Fe^{III}Cp*₂]⁺ for the **FO** polymorph at 19 K (a), the **MM** polymorph at 17 K (**MM_{LT}**) (b) and 300 K (**MM_{RT}**) (c), and for ferromagnetic [FeCp*₂][TCNE] at 12 K¹⁰ (d) that belong to the $\sim D_{5h}$, D_{5d} , D_5 , and D_{5h} point groups, respectively.

Structure of **MM_{LT}**

The structure of **MM** at 17 K (**MM_{LT}**) belongs to the same $P\bar{1}$ space group, it was not isomorphous with the previously reported 167-K structure for **MM**,⁶ Table 1, and has a 1.9% volume contraction

and the intrachain Fe \cdots Fe separation decreases by 1.0% to 10.439 Å, Table 2. Each chain is surrounded by 6 parallel chains, Figure S7, forming two identical pairs out-of-registry nearest neighbor chains, **I-II** (and **I-II'**) and **I-III** (and **I-III'**) separated by 9.245 and 8.389 Å, respectively, and one pair of in-registry nearest neighbor chains **I-IV** (and **I-IV'**) separated by 8.631 Å, Figure S7, Table 2. The shortest interchain Fe \cdots Fe, Fe \cdots N, and N \cdots N separations are 8.631, 5.225, and 3.729 Å, respectively, Table 2. The [Fe^{III}Cp*₂]⁺ cation has a Fe-C distance of 2.125 Å, and Fe \cdots C₅-ring centroid of 1.731 Å, with the two Cp* rings being staggered, Figure 3b. Thus, the FeC₁₀ core has *D*_{5d} symmetry.

As part of the structural investigation of **MM** at low temperature, the room temperature unit cell was determined, and although **MM**_{RT} had the same *P* $\bar{1}$ space group, it was not isomorphous with the previously reported 167-K structure for **MM**,⁶ Table 1. Above 226 K, the unit cell volume is double of that observed at low temperature because the Fe atom is no longer on an inversion site, and, the Cp* rings are crystallographically independent of one another because the irreducible cell includes all atoms of each molecule in the formula unit; at room temperature the Cp* rings are rotated by 15° relative to the eclipsed configuration. The [Fe^{III}Cp*₂]⁺ cation has a Fe-C distance of 2.096 Å, and Fe \cdots C₅-ring centroid of 1.733 Å, with the two Cp* rings being staggered with a 14.4° dihedral angle, Figure 3c. Thus, the FeC₁₀ core has *D*₅ symmetry. The relative orientation between the [FeCp*₂]⁺ and [TCNQ]⁻ differs for the room temperature **MM**_{RT} and low temperature **FO** and **MM**_{LT} structures, Figure 4. The most symmetric cation occurs for **MM**_{LT} at 17 K, Figure 4b.

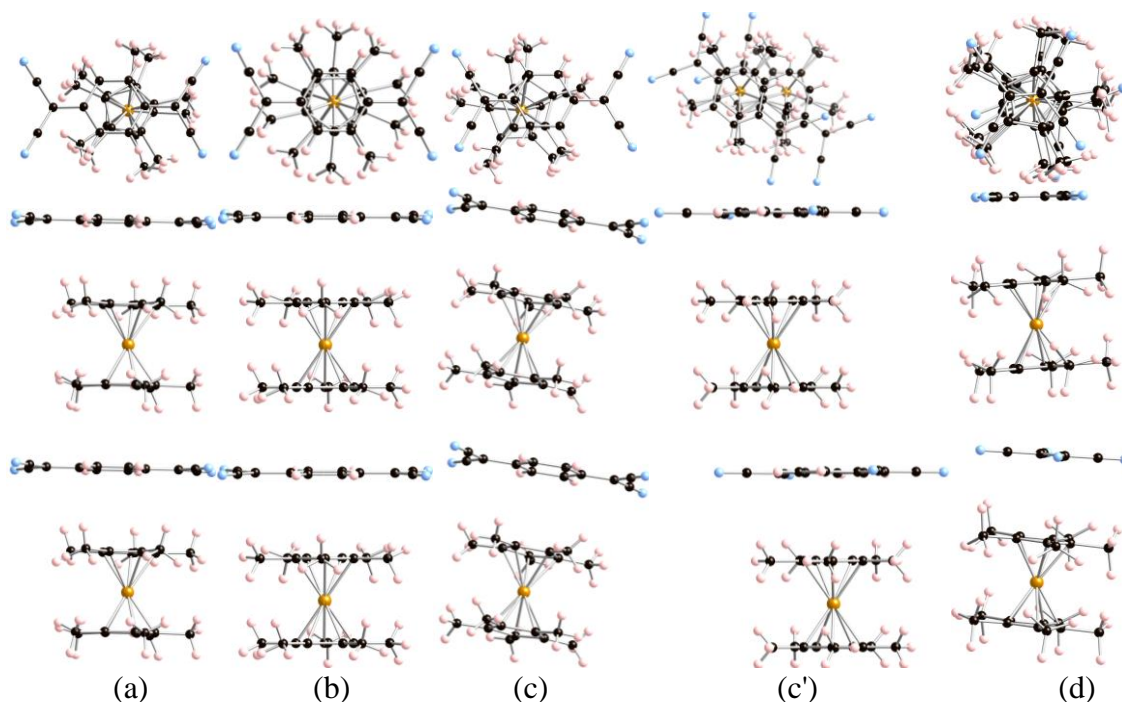


Figure 4. Top (above) and side (below) views of for the chain motif for **MM** at 300 (**MM_{RT}**) (a) and 17 K (**MM_{LT}**) (b), for **FO** at 19 K (c, c'), and for [FeCp*₂][TCNE] (d). The TCNQ and Cp* planes are not perpendicular to the chain axis for (c), and (c') shows the side and top views looking normal to these planes. For (a), (b), and (c/c') the iron atoms are eclipsed and the exo-C-C TCNQ bonds are parallel to the top of the page when rotated by 90°.

Comparison of the low temperature **FO**, **MM**, and [FeCp*₂][TCNE] structures

FO, **MM**, and [FeCp*₂][TCNE] each possess chains of alternating cations and anions and each chain is surrounded by two in-registry and four out-of-registry chains as described above, Figures S5, S6, S7, S8, and 4. The main structural difference between **FO** and **MM_{LT}** polymorphs of [FeCp*₂][TCNQ] at low temperature occurs for the in-registry [TCNQ]^{•••}[TCNQ]^{•••} interactions, Figures S6 (**I-II**) and S8 (**I-IV**), with the **MM_{LT}** polymorph having a 10.0% shorter separation (3.729 Å) with respect to the **FO** polymorph (4.143 Å), Table 2. Also, the intrachain Fe^{•••}Fe separation is 2.8% shorter for **MM_{LT}** (10.439 Å) than for **FO** (10.738 Å). While the N^{•••}N separation is longer for **FO**, the in-registry interchain and Fe^{•••}Fe separations are 3.8 and 1.0% shorter, respectively, for **FO**, Table 2. Likewise, the shortest out-of-registry interchain, Fe^{•••}Fe, and Fe^{•••}N separations are 1.6, 3.2, and 9.1% shorter, respectively, for **FO**.

The biggest difference between **FO** and [FeCp*₂][TCNE], of course, is that *D*_{2h} [TCNQ]^{•••} is about twice the size of the almost square *D*_{2h} [TCNE]^{•••}. Thus, reduced interchain separations

are anticipated for $[\text{FeCp}^*_2][\text{TCNE}]$. While the reduced size of $[\text{TCNE}]^-$ should not directly affect the intrachain separation, it however, it is 10.738 Å for **FO**; 3.0% longer with respect to $[\text{FeCp}^*_2][\text{TCNE}]$ (10.415 Å), and it is an 0.23% shorter than for **MM_{LT}** (10.439 Å). The smaller $[\text{TCNE}]^-$ leads to a 17.8% decrease in the N•••N separation to 3.408 Å from 4.143 Å in **FO**, and 8.6% decrease with respect to **MM_{LT}** (3.729 Å), as expected. Likewise, the shortest out-of-registry interchain, Fe•••Fe, and Fe•••N separations are 1.6, 3.2, and 9.1% shorter, respectively, for **FO**. Each of the in- and out-of-registry Fe•••Fe and interchain separations for $[\text{FeCp}^*_2][\text{TCNE}]$ are reduced from 1.5 to 10.9% with respect to **FO**, and by 4.9 to 12.3% with respect to **MM_{LT}**. The out-of-registry Fe•••N separation increases from 4.789 Å by 5.3% to 5.042 Å for $[\text{FeCp}^*_2][\text{TCNE}]$, and this is attributed to the almost square nature of $[\text{TCNE}]^-$ enabling it to adopt a differently rotated orientation; however, this separation decreases by 3.5% from the 5.225 Å observed for **MM_{LT}**.

Thermal behavior of MM

A DSC study confirmed the phase transition upon warming above -55 °C, Figure 5. The transition temperature (T_{warm}) was determined from extrapolation of the most linear portion of the onset of absorption in the heat flow to an approximated baseline established from the internal standard heat flow. A slight variation was observed in this value with that observed upon cooling (T_{cool}), and these differences were found to depend on the temperature scan rate and was determined to be an artifact of finite temperature scan rates. The T_{warm} and enthalpy of transition were determined to be 226.5 ± 0.4 K (-46.7 ± 0.4 °C) and 0.68 ± 0.04 kJ/mol (0.16 ± 0.01 kcal/mol), respectively, Figure 5. The transition was found to be robust under successive temperature cycles and for multiple samples. Calorimetric studies of the related MnCp^*_2 ²⁶ and $[\text{FeCp}^*_2][\text{TCNE}]$ ^{10,27} revealed structural transitions at similar temperatures. While MnCp^*_2 displayed a peak between 255 and 238 K, which was attributed to slipping of MnCp^*_2 units within a chain,²⁶ $[\text{FeCp}^*_2][\text{TCNE}]$ exhibited anomalies in the adiabatic heat capacity at 248.7 and 281.8 K.²⁷ The structural similarities between $[\text{FeCp}^*_2][\text{TCNE}]$ and **MM** suggest that the transition, Figure 5, may be analogous to that observed for $[\text{FeCp}^*_2][\text{TCNE}]$. The reported enthalpy for the $[\text{FeCp}^*_2][\text{TCNE}]$ transition (3.32 kJ/mol) is significantly larger than reported for **MM**, but includes the neighboring anomaly at 281.8 K, which adds substantially to the enthalpy.²⁷ The transition at 248.7 K for $[\text{FeCp}^*_2][\text{TCNE}]$ was classified as an order-disorder type on the basis of entropy,²⁷ which was

consistent with later temperature dependent diffraction studies.¹¹ The absence of disorder in diffraction data of **MM** indicate that the behavior observed at 226.5 K is more likely to resemble that of MnCp^*_2 .⁶ However, unlike for MnCp^*_2 where an anomaly occurs in the temperature dependent magnetic susceptibility data,⁶ there is no evidence of such a transition for either **MM** or $[\text{FeCp}^*_2][\text{TCNE}]$. The investigation of the 70 ± 10 K **MM** to **MM_{LT}** phase transition was beyond the limits of our DSC and thus unfortunately could not be studied.

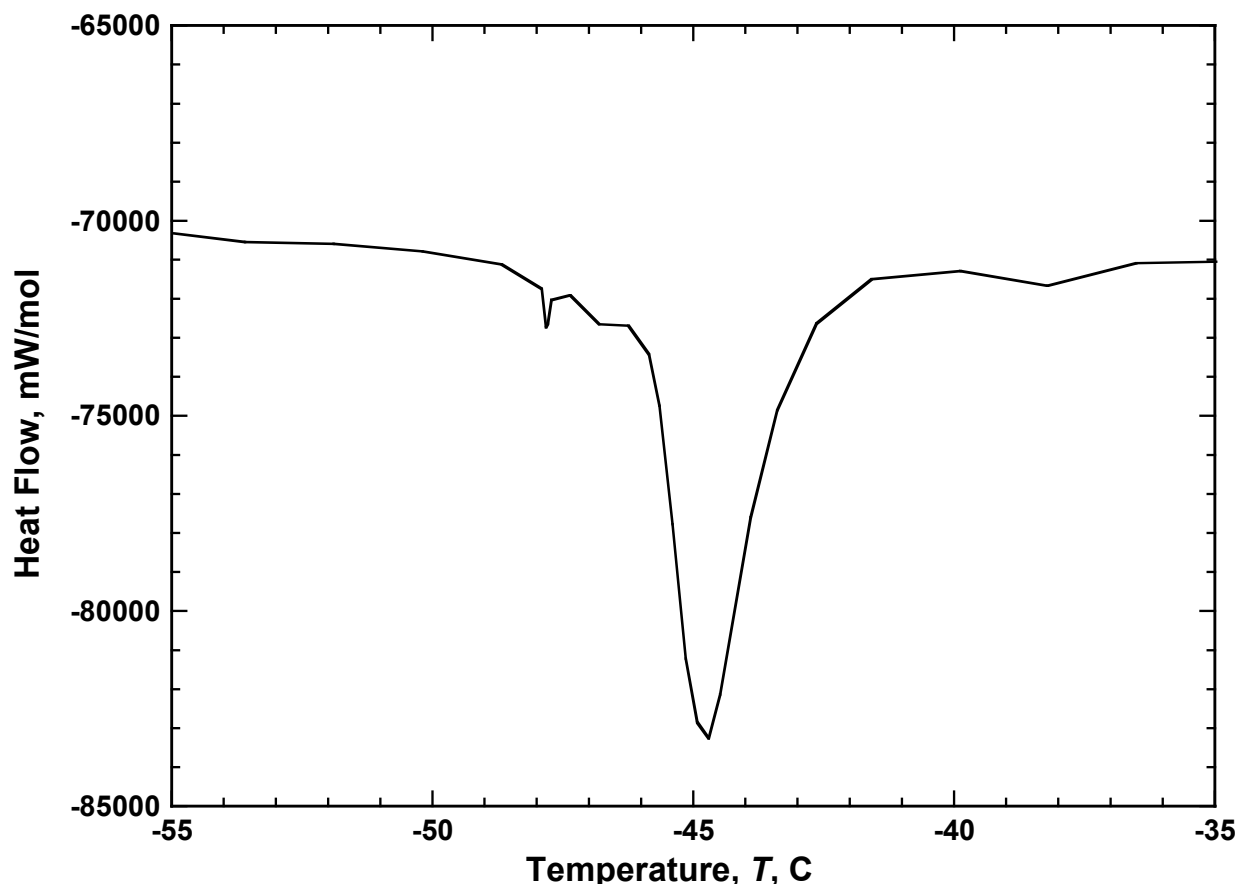


Figure 5. Heat flow of a representative sample of **MM** upon warming.

Spin coupling analysis for the FO and MM polymorphs of $[\text{FeCp}^*_2][\text{TCNQ}]$ and $[\text{FeCp}^*_2][\text{TCNE}]$

Methodological details

The spin-coupling interactions, J_{ij} , between the nearest neighbor $[\text{FeCp}_2]^{*+} \cdots [\text{TCNQ}]^-$, $[\text{FeCp}_2]^{*+} \cdots [\text{FeCp}_2]^{*+}$, and $[\text{TCNQ}]^- \cdots [\text{TCNQ}]^-$ radical pairs present in the **FO** and **MM_{LT}** polymorphs were evaluated using the $H = -2J_{ij}S_i \cdot S_j$ Heisenberg Hamiltonian. Since each of these

spin-containing units are doublets, values of J_{ij} for all symmetry-unique pairs of spin-containing units were computed as $J_{ij} = (E(S)_{ij} - E(T)_{ij})/2$, where $E(S)_{ij}$ and $E(T)_{ij}$ are the energies of the lowest-energy singlet and triplet states for the ij pair. The wave-function based RASSCF methodology,²⁸ as implemented in the MOLCAS package,²⁹ was used to calculate these energies. To ensure the introduction of all correlation energy involved in the singlet-triplet gaps, all p and d orbitals (double-shell) in the restricted active space through orbital localization technique are included. In all energy calculations, the Madelung field effect has been incorporated introducing ~1500-point charges surrounding the ab-initio calculated dimer. Those charges were obtained for the $[\text{FeCp}_2]^{2+}$ and $[\text{TCNQ}]^-$ ions at the DFT level.

The restricted active space used for the $[\text{FeCp}^*_2]^{2+}\cdots[\text{TCNQ}]^-$ dimers is (34, 2, 2; 15, 3, 18)³⁰ and it is based on a (34, 36) active space. (Figure S9 includes the scheme of the RASSCF methodology.) The orbitals included in the restricted active space are: (a) the five orbitals of $[\text{FeCp}_2]^{2+}$ of dominating Fe character, which possess five electrons, (b) the $[\text{TCNQ}]^-$ SOMO orbital, (c) a second shell of empty d orbitals on Fe intended to allow the $d-d$ correlation (d -doubling), and (d) all Cp^* and $[\text{TCNQ}]^-$ π orbitals. MOs for $[\text{FeCp}^*_2]^{2+}\cdots[\text{TCNQ}]^-$ dimers are shown in Figure S10. In contrast, the restricted active space used for the $[\text{TCNQ}]^- \cdots [\text{TCNQ}]^-$ dimers is (34, 2, 2; 16, 2, 14) and is based on a (34, 32) active space. The orbitals included are all of the $[\text{TCNQ}]^-$ π orbitals (Figure S11). Finally, the restricted active space used to calculate the magnetic coupling between the $[\text{FeCp}^*_2]^{2+}\cdots[\text{FeCp}^*_2]^{2+}$ radical pairs is (34, 2, 2; 14, 4, 22), and is based on a (34,22) active space. The orbitals included are the d orbitals (double-shell) of the Fe atom and all π orbitals of the Cp^* units (Figure S12). Therefore, the three RAS active spaces are of similar accuracy. All RASSCF calculations were performed using the atomic natural orbital ANO-RCC basis sets.³¹ The contractions used were: [4s3p] for the C atoms of the Cp^* rings, [5s4p] for the C and N atoms of the $[\text{TCNQ}]^-$, [6s4p3d1f] for the Fe atoms, and [2s] for the H atoms.

SOMOs

The ground state of $[\text{FeCp}^*_2]^{2+}$ is a doublet that has a strong multi-referent character involving two degenerated d-dominated MOs³² of $[\text{FeCp}^*_2]^{2+}$ (Figure 6a). It is thus a common practice to use state-average MCSCF computations for the $[\text{FeCp}^*_2]^{2+}$ doublet considering two pseudo-degenerate states^{10,33} including all five Fe d orbitals with its electrons. This near degeneration dominated by

the d-MOs present in $[\text{FeCp}^*_2]^+$ doublet is maintained in the $[\text{FeCp}^*_2]^+\cdots[\text{TCNQ}]^-$ pairs (Figure 6b). Indeed, an analysis of the occupation of the orbitals for a $[\text{FeCp}^*_2]^+\cdots[\text{TCNQ}]^-$ pair excised from the stacks shows that three SOMOs have occupations of 1.5, 1.5 and 1.0 (Figure 7). The two SOMOs with occupations of 1.5 correspond to the non-bonding d_{xy} and $d_{x^2-y^2}$ orbitals of Fe, while the remaining SOMO with an occupation of 1.0 corresponds to the bonding combination between of the d_{xz} orbital of Fe and the π^* orbital of $[\text{TCNQ}]^-$ {and also in $[\text{TCNE}]^-$ }.¹⁰ Note that a 1.5, 1.5, 1.0 occupation is typical for a multireference wavefunction, where two configurations in which the three SOMOs of Figure 7 have occupations 2, 1, 1 and 1, 2, 1 and each are combined with a 50% weight.

As a consequence, two pseudo-degenerate singlets and two pseudo-degenerate triplets have to be considered. Likewise, four pseudo-degenerate singlets and four pseudo-degenerate triplets were considered for the $[\text{FeCp}^*_2]^{++}\cdots[\text{FeCp}^*_2]^+$ radical pairs. Similar conclusions were obtained for the singlet and triplet states of $[\text{FeCp}^*_2]^+\cdots[\text{TCNE}]^-$.¹⁰

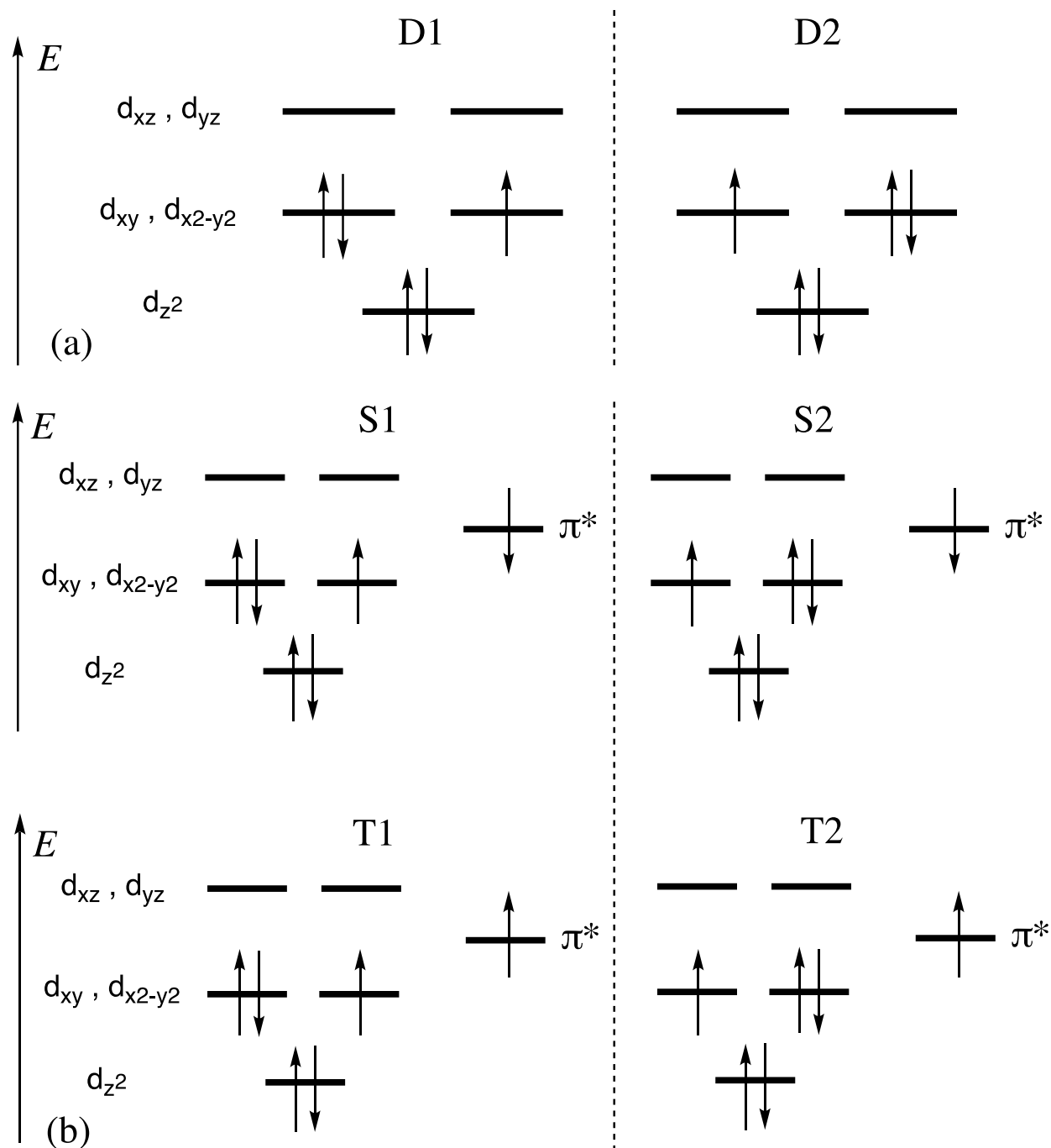


Figure 6. Qualitative MO diagram describing: (a) the state of lowest energy for the doublet (D1 and D2) $[\text{FeCp}^*_2]^+$ radical cation; (b) the state of lowest energy for the doubly degenerate triplet states (T1 and T2) for $[\text{FeCp}^*_2]^+[\text{TCNQ}]^-$, two states that are more stable than their associated doubly degenerate S1 and S2 singlets states. The qualitative MO diagram for the $[\text{FeCp}^*_2]^+\cdots[\text{TCNE}]^-$ pair is similar to that computed here for the $[\text{FeCp}^*_2]^+\cdots[\text{TCNQ}]^-$ radical pair.

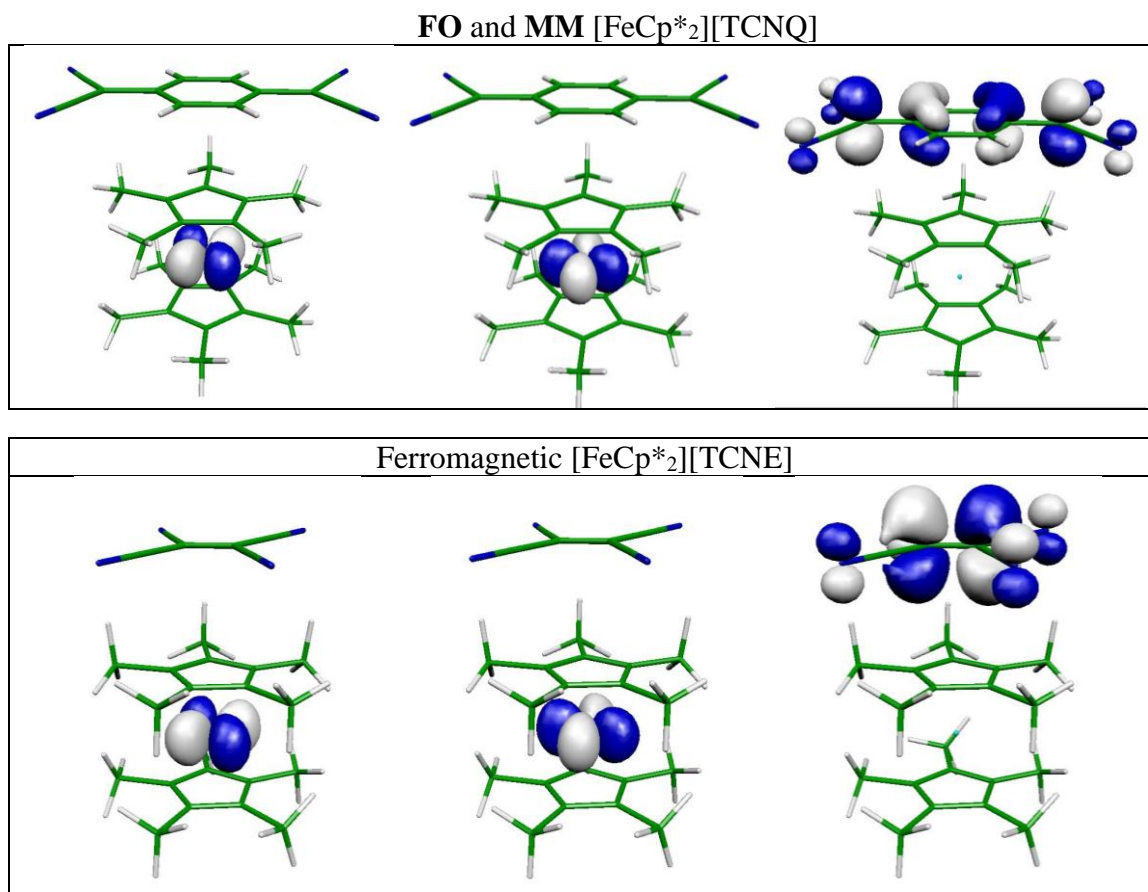


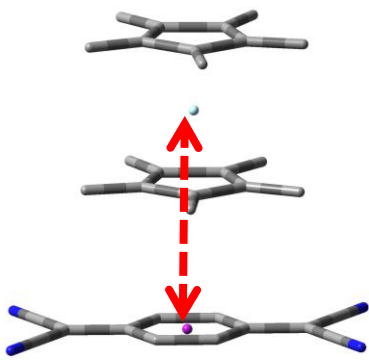
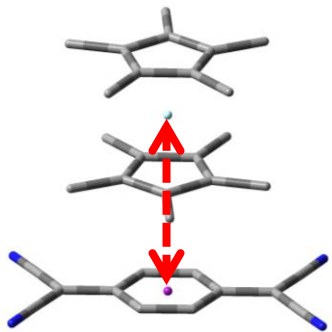
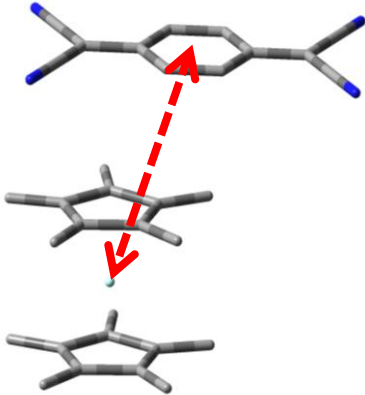
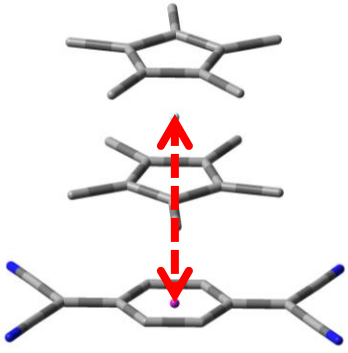
Figure 7. Shape of the three SOMOs computed at the B3LYP/6-31g(d) level for [FeCp*₂][TCNQ] (top) extracted from the **FO** and **MMLT** structures (the same results are obtained in both cases) and for [FeCp*₂][TCNE] (bottom) (the isosurface of 0.02 atomic units is plotted, white for positive values and blue for negative values). Their electron occupation (left to right) is 1.5:1.5:1.0 atomic unit (electrons). The shape and occupation of the three [FeCp*₂][TCNE] SOMO orbitals are identical to that previously reported using the CASSCF(8,7) wave function¹⁰ (a different isosurface is presented for a clearer view of the nodal structure).

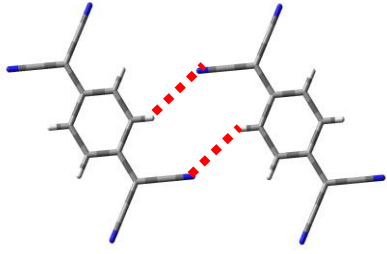
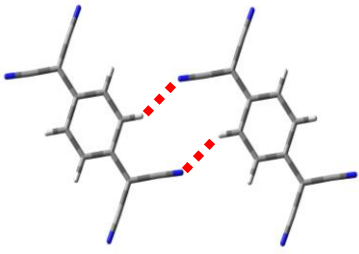
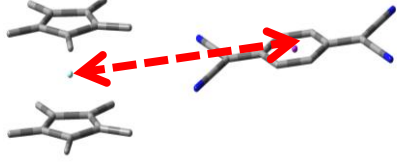
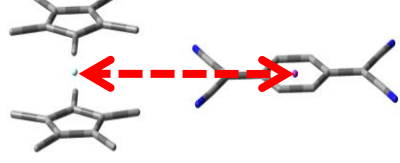
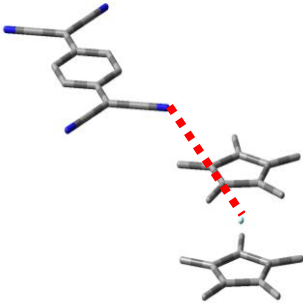
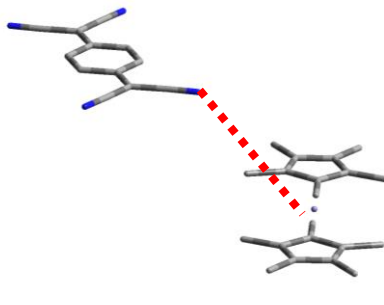
Results of the spin coupling analysis

The J_{ij} values were evaluated for each symmetry-unique radical pair found in the crystal structures of the **FO** and **MMLT** polymorphs of [FeCp*₂][TCNQ] determined at 18 ± 1 K. The five nearest neighbor interactions for which the associated J_{ij} is different from zero in at least one of the polymorphs are shown in Table 3. The differences in the relative orientations present for the **FO** and **MMLT** polymorphs is presented in Figure 8. All the J_{ij} couplings between the nearest neighbor

$[\text{FeCp}^*_2]^+\cdots[\text{FeCp}^*_2]^+$ pairs were computed to be negligible and will therefore not be further considered.

Table 3. Computed nearest-neighbor magnetic exchange interactions, J_{ij} (cm^{-1}), for the $[\text{FeCp}^*_2]^+\cdots[\text{TCNQ}]^-$, $[\text{FeCp}^*_2]^+\cdots[\text{FeCp}^*_2]^+$, and $[\text{TCNQ}]^-\cdots[\text{TCNQ}]^-$ nearest-neighbor interactions present for the **FO** and **MM_{LT}** polymorphs of $[\text{FeCp}^*_2]^+[\text{TCNQ}]^-$ for which $|J_{ij}| \geq 0.1 \text{ cm}^{-1}$ in at least one of the polymorphs. Note that none of the $[\text{FeCp}^*_2]^+\cdots[\text{FeCp}^*_2]^+$ have a $|J_{ij}| \geq 0.1 \text{ cm}^{-1}$. Z is the number of equivalent interactions in the unit cell, and C is the centroid of the ion.

		FO $[\text{FeCp}^*_2][\text{TCNQ}]$		MM _{LT} $[\text{FeCp}^*_2][\text{TCNQ}]$		
	J , cm^{-1}	Z	Interaction	J , cm^{-1}	Z	Interaction
J_1	5.2	4		6.5	2	
			$\text{Fe}\cdots\text{C}(\text{TCNQ}) = 5.311 \text{ \AA}$ $\text{C}(\text{Cp}^*)\cdots\text{C}(\text{TCNQ}) = 3.573 \text{ \AA}$			$\text{Fe}\cdots\text{C}(\text{TCNQ}) = 5.219 \text{ \AA}$ $\text{C}(\text{Cp}^*)\cdots\text{C}(\text{TCNQ}) = 3.505 \text{ \AA}$
J_2	4.7	4		J_2 $=J_1$		
			$\text{Fe}\cdots\text{C}(\text{TCNQ}) = 5.667 \text{ \AA}$ $\text{C}(\text{Cp}^*)\cdots\text{C}(\text{TCNQ}) = 3.570 \text{ \AA}$			$\text{Fe}\cdots\text{C}(\text{TCNQ}) = 5.219 \text{ \AA}$ $\text{C}(\text{Cp}^*)\cdots\text{C}(\text{TCNQ}) = 3.505 \text{ \AA}$

J_3	0.2	4		-0.1	1	
			$N \cdots H = 2.820 \text{ \AA}$			$N \cdots H = 2.465 \text{ \AA}$
J_4	0.1	4		0.0		
			$Fe \cdots C(\text{TCNQ}) = 9.389 \text{ \AA}$ $C(\text{Cp}^*) \cdots C(\text{TCNQ}) = 3.732 \text{ \AA}$			$Fe \cdots C(\text{TCNQ}) = 9.245 \text{ \AA}$ $C(\text{Cp}^*) \cdots C(\text{TCNQ}) = 3.737 \text{ \AA}$
J_5	0.1	4		0.0		
			$N(\text{TCNQ}) \cdots C(\text{Cp}^*) = 3.696 \text{ \AA}$			$N(\text{TCNQ}) \cdots C(\text{Cp}^*) = 3.782 \text{ \AA}$

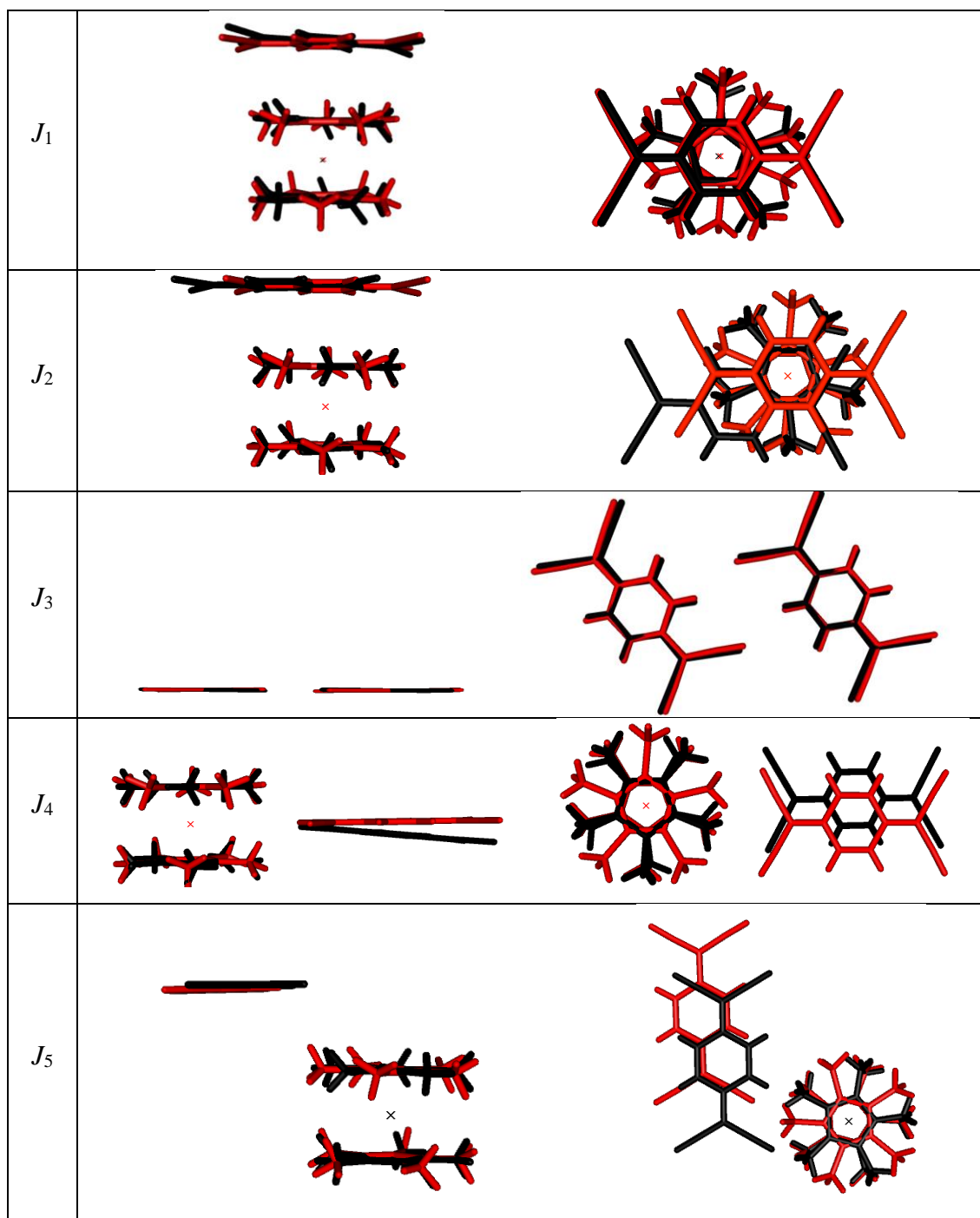


Figure 8. Superposition of the $[\text{FeCp}^*_2]^+ \cdots [\text{TCNQ}]^-$ interactions for both **FO** (black) and **MMLT** (red) polymorphs.

The alternating $[\text{FeCp}^*_2]^+$ and $[\text{TCNQ}]^-$ ions present within each chain present for **FO** and **MMLT** (Figure 8) are computed to have ferromagnetic coupling, *i.e.* $J > 0$, and be the strongest nearest neighbor magnetic coupling for each polymorph. The average intrachain

$[\text{FeCp}^*_2]^+ \cdots [\text{TCNQ}]^-$ interaction is computed to be 6.5 cm^{-1} for **MM_{LT}**, which on average is 24% lower for **FO**, Table 3. Note that the intrachain interaction for **MM_{LT}** has higher symmetry than for **FO**; thus, the two different 5.2 and 4.7 cm^{-1} interactions (J_1 and J_2) for **FO** become equivalent (6.5 cm^{-1}) for **MM_{LT}**, Table 3. This, in part, is due to the 2.8% shorter separation for Fe \cdots Fe separation for **MM_{LT}** with respect to **FO**, and differing orientations (Figure 8).

The MOs shown in Figures 7 and 9 provide a rationale for the ferromagnetic nature of the intrachain couplings. It should be noted that the degenerate SOMOs of ferrocenium, which are essentially localized on the d_{xy} and $d_{x^2-y^2}$ orbitals of the Fe ion, are nearly orthogonal by symmetry to the SOMO of $[\text{TCNQ}]^-$. In fact, when the SOMOs of the intrachain $[\text{FeCp}^*_2]^+ \cdots [\text{TCNQ}]^-$ pairs are plotted using a very small threshold for the electron density (see Figure 9) it is observed that the d_{xy} and $d_{x^2-y^2}$ -centered orbitals do not combine with the π^* orbital of $[\text{TCNQ}]^-$. The vanishingly small overlap between the degenerate SOMOs of ferrocenium and the SOMO of $[\text{TCNQ}]^-$ (Table 4) leads to a negligible antiferromagnetic component of the intrachain spin coupling. Second, the shape of the SOMO of the $[\text{FeCp}^*_2]^+ \cdots [\text{TCNQ}]^-$ pair with an occupation of 1 displayed in Figure 9 explains the significant value of its ferromagnetic coupling. Specifically, this SOMO demonstrates that there is a partial charge transfer from the π^* orbital of $[\text{TCNQ}]^-$ to one of the degenerate virtual orbitals of $[\text{FeCp}^*_2]^+$ (d_{xz} orbital). Such partial charge transfer is enabled by the delocalization of the d_{xz} orbital over the C_p rings, which results in a non-negligible overlap between the SOMO of $[\text{TCNQ}]^-$ and the d_{xz} orbital of the Fe ion (Table 4). The partial occupation of one of the virtual orbitals of ferrocenium favors the ferromagnetic coupling by virtue of Hund's rule.

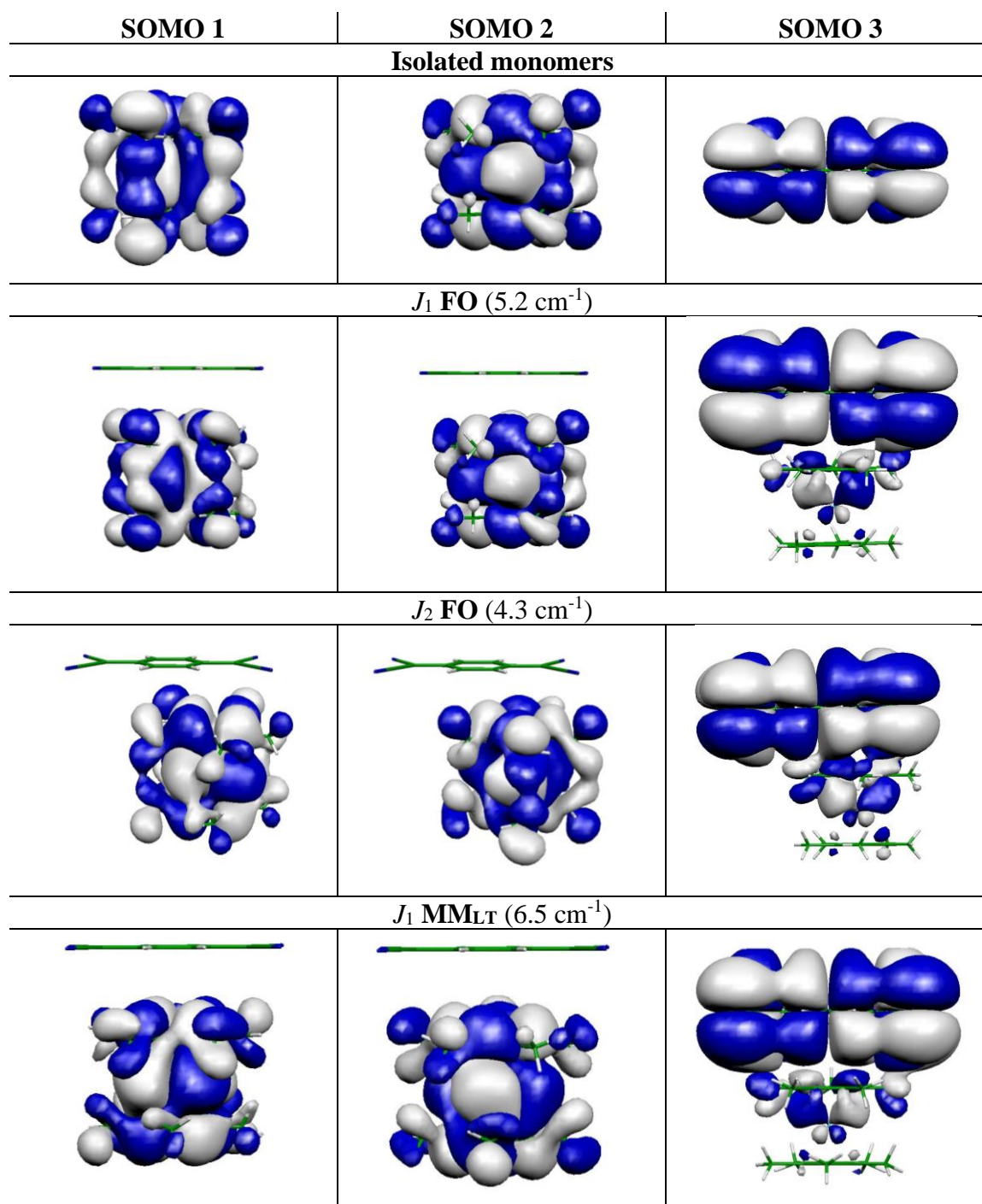


Figure 9. RASSCF SOMO orbitals of J_1 (5.2 cm^{-1}) and J_2 (4.3 cm^{-1}) of the FO and J_1 (6.5 cm^{-1}) for MM_{LT}. Triplet orbitals in all cases. All the orbitals have been plotted using a cutoff of 0.002.

Table 4. Overlap in atomic units between the [TCNQ]⁻ SOMO and: (a) one SOMO of [FeCp*₂]^{•+}, (b) and (c) the two virtual antibonding Cp*-Fe(d) orbitals. The results are for the J_1 and J_2 dimers for both the **FO** and the **MM_{LT}** phases of [FeCp*₂][TCNQ]. The orbitals used are from a ROB3LYP/6-31g(d) calculation.

Polymorph		J_i	(a)	(b)	(c)
J_1	FO	5.2	0.00052	0.00119	-0.00904
J_2	FO	4.3	0.00245	0.00271	0.00935
$J_1 = J_2$	MM_{LT}	6.5	-0.04144	0.00914	-0.01104

In both of the **MM_{LT}** and **FO** polymorphs, there are 5 symmetry unique J_n ($n = 1, 2, 3, 4, 5$) magnetic interactions (Table 3; Figure 8): (1) J_1, J_2 , and J_3 are the three strongest magnetically coupled radical pairs and J_4 and J_5 , whose average strength ($\sim 5 \text{ cm}^{-1}$) is nearly twenty times weaker than that for J_1, J_2 and J_3 , the latter are the dominating magnetic interactions. For **MM_{LT}** and **FO** the dominating interactions interconnect the [FeCp*₂]^{•+} radical cations and [TCNQ]⁻ radical anions by a network of nearly parallel 1D chains, while the J_4 and J_5 interactions interconnect these 1D chains among their surrounding chains; thus, giving rise to a 3D network of magnetic interactions. None of the computed nearest neighbor couplings are negative, *i.e.* antiferromagnetic, and this is in agreement with observed ferromagnetic ground state for the **FO** polymorph. Furthermore, there are two [FeCp*₂]^{•+}•••[TCNQ]⁻ interactions computed to have a 0.1 cm^{-1} ferromagnetic interaction for **FO**, which are reduced to 0.0 cm^{-1} for **MM_{LT}**, Table 3.

As discussed above, the main structural difference between **FO** and **MM_{LT}** lies in the 10.0% shorter [TCNQ][•]•••[TCNQ]⁻ (J_3) separations for **MM_{LT}**, Table 2. This along with the nominal change in relative orientations leads to a computed change from the ferromagnetic interaction (0.2 cm^{-1}) due to the near orbital orthogonality for **FO** (vide supra) to an antiferromagnetic interaction (-0.1 cm^{-1}) and is in accord with **MM_{LT}** having an antiferromagnetic ground state. The small values of the spin couplings due to weak lateral orbital interactions, together with the change in their sign in going from **FO** to **MM_{LT}**, indicate that the sign and value of the spin coupling in these pairs of radicals are governed by a delicate interplay of the overlap between SOMOs (which favors an antiferromagnetic coupling) and the exchange integral between SOMOs (which favors a ferromagnetic coupling). The antiferromagnetic interaction in the **MM_{LT}**

polymorph is consistent with its shorter separations and the concomitant increase in the overlap between SOMOs (Figure 10), which results in the antiferromagnetic contribution of J_3 prevailing over the ferromagnetic contribution.

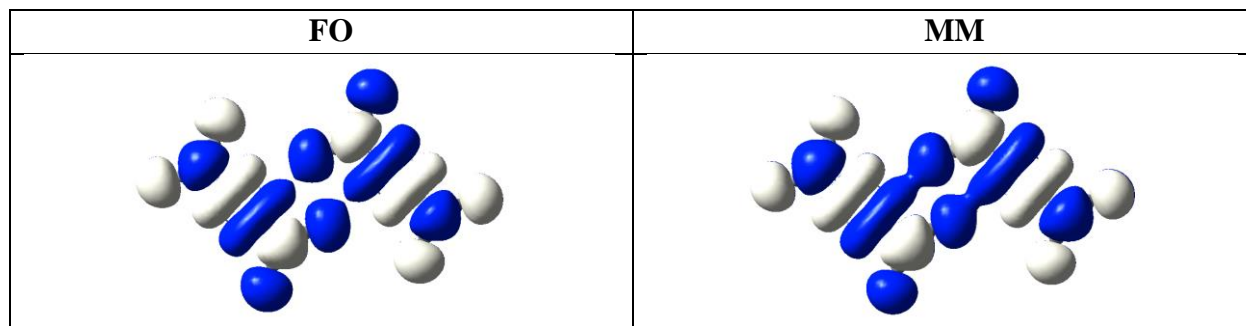


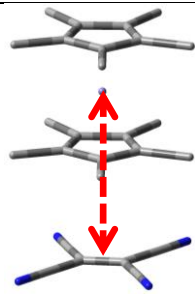
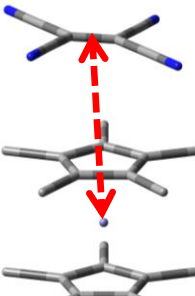
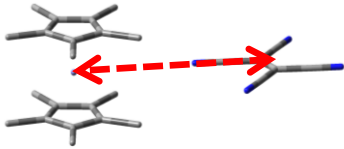
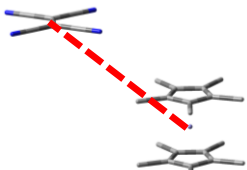
Figure 10. Top view of the bonding SOMO of the $[\text{TCNQ}]^{\bullet\bullet\bullet}[\text{TCNQ}]^{\bullet-}$ pairs in the **FO** and **MM_{LT}** polymorphs. The two SOMOs (resulting from a ROB3LYP/6-311+G(d) calculation) have been plotted using a cutoff of 0.0045.

While the $[\text{FeCp}^*_2][\text{TCNQ}]$ (**FO**) and the $[\text{FeCp}^*_2][\text{TCNE}]$ ferromagnets have differing magnetic topologies, Figure S13, both have a similar intrachain structure, Figure 4, and the two different ferromagnetic couplings (27.9 and 45.3 cm^{-1}) (Table 5) for $[\text{FeCp}^*_2][\text{TCNE}]$ average 36.6 cm^{-1} , which is 7.4 times larger than for **FO** $[\text{FeCp}^*_2][\text{TCNQ}]$. This enhanced ferromagnetic coupling is attributed to the smaller size and concomitant greater spin density for $[\text{TCNE}]^{\bullet-}$ with respect to $[\text{TCNQ}]^{\bullet-}$ (Figure 7), and a higher T_c {4.8 K for $[\text{FeCp}^*_2][\text{TCNE}]$; 3.1 K for **FO**} that cannot be accounted for from the 3% reduced intrachain separation.

To explain the bulk magnetic behaviors for the **FO** and **MM_{LT}** polymorphs of $[\text{FeCp}^*_2][\text{TCNQ}]$ and $[\text{FeCp}^*_2][\text{TCNE}]$, magnetic dipolar interactions may play an additional, but essential, contribution. Magnetic dipolar interactions should have magnitude similar to the extremely low interchain J values, but the cooperative nature could strengthen their relevance.

Table 5. Computed nearest-neighbor magnetic exchange interactions, J_{ij} , for the $[\text{FeCp}^*_2]^{\bullet\bullet\bullet}[\text{TCNE}]^{\bullet-}$, $[\text{FeCp}^*_2]^{\bullet\bullet\bullet}[\text{FeCp}^*_2]^{\bullet}$, and $[\text{TCNE}]^{\bullet-}\bullet\bullet\bullet[\text{TCNE}]^{\bullet-}$ nearest neighbor pairs present for the ferromagnetic $[\text{FeCp}^*_2]^{\bullet\bullet\bullet}[\text{TCNE}]^{\bullet-}$. Z is the number of equivalent interactions in the unit cell and C is the centroid of the ion. Except for the value of J_3 , the rest of J_{ij} values in the table

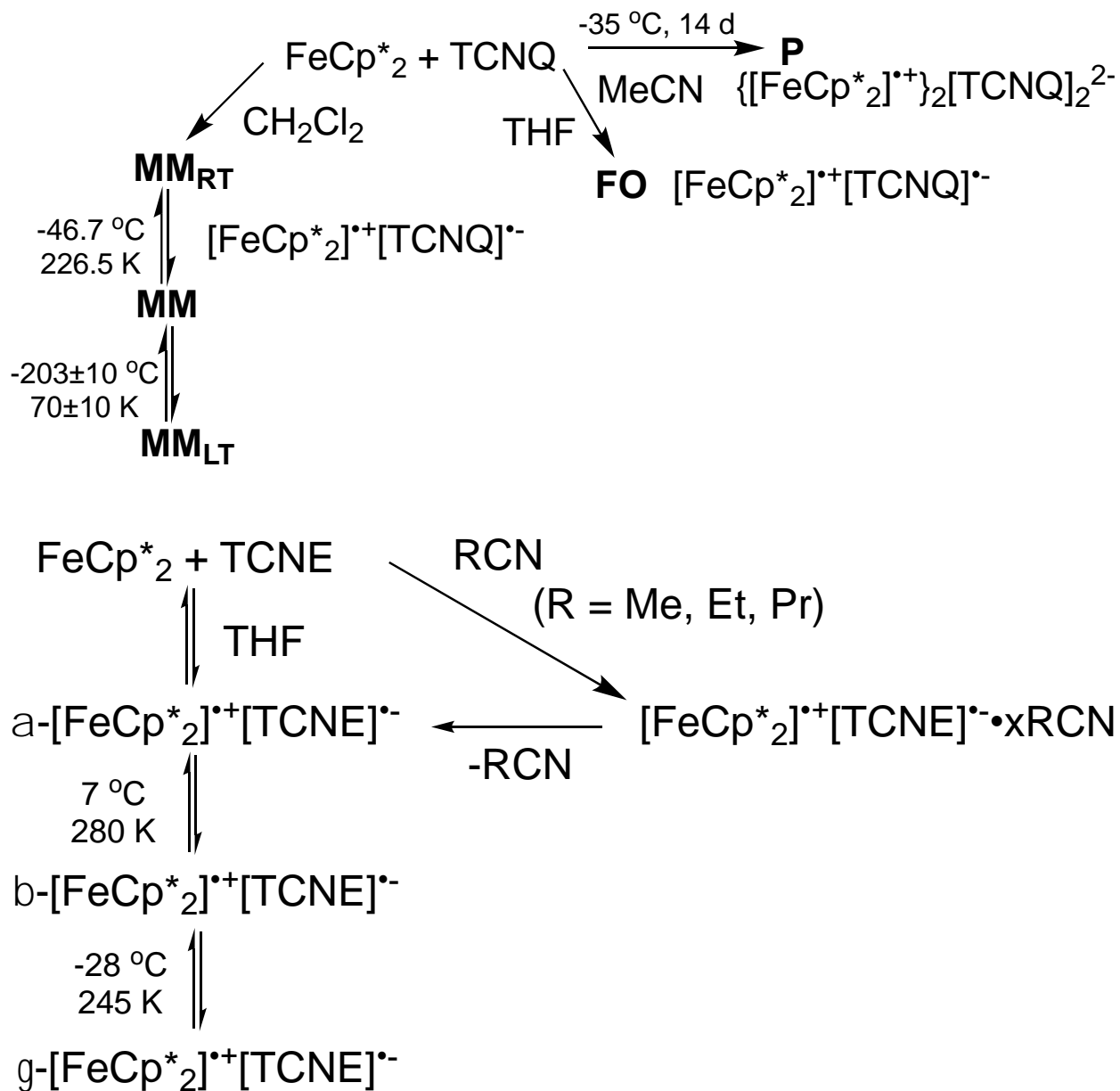
correspond to the values reported in Ref. 10. J_3 has been recalculated using the same RASSCF methodology used herein.

J_{ij}	J, cm^{-1}	Z	Ferromagnetic $[\text{FeCp}^*_2][\text{TCNE}]$
J_1	45.3	4	
			$\text{Fe} \cdots \text{X}(\text{TCNE}) = 5.323 \text{ \AA}$ $\text{C}(\text{Cp}^*) \cdots \text{C}(\text{TCNE}) = 3.650 \text{ \AA}$
J_2	27.9	4	
			$\text{Fe} \cdots \text{C}(\text{TCNE}) = 5.209 \text{ \AA}$ $\text{C}(\text{Cp}^*) \cdots \text{C}(\text{TCNE}) = 3.464 \text{ \AA}$
J_3	0.0	2	
			$\text{C}(\text{TCNE}) \cdots \text{C}(\text{TCNE}) = 8.321 \text{ \AA}$
J_4	0.2 cm^{-1}	4	
			$\text{Fe} \cdots \text{C}(\text{TCNE}) = 7.804 \text{ \AA}$ $\text{C}(\text{Cp}^*) \cdots \text{C}(\text{TCNE}) = 3.576 \text{ \AA}$
J_5	0.0	4	
			$\text{N}(\text{TCNQ}) \cdots \text{C}(\text{Cp}^*) = 3.890 \text{ \AA}$

Conclusion

As summarized by Scheme 1, $[\text{FeCp}^*_2][\text{TCNQ}]$ forms five phases, namely, a paramagnet (**P**) possessing $S = 1/2$ $[\text{FeCp}^*_2]^{*+}$ and $S = 0$ $[\text{TCNQ}]_2^{2-}$ ions, and **FO** and **MM** polymorphs with the latter having differing structures at room (**MM_{RT}**) and at low temperatures (**MM_{LT}**), than below 167 K; nonetheless, these four 1-D structures possess parallel $\cdots[\text{FeCp}^*_2]^{*+}\cdots[\text{TCNQ}]_2^{2-}\cdots[\text{FeCp}^*_2]^{*+}\cdots[\text{TCNQ}]_2^{2-}\cdots$ 1-D chains with differing relative orientations. The **FO** and three **MM** phases of $[\text{FeCp}^*_2][\text{TCNQ}]$ and ferromagnetic $[\text{FeCp}^*_2][\text{TCNE}]$ possess similar inter- and intrachain structures possessing alternating $S = 1/2$ $[\text{FeCp}^*_2]^{*+}$ and $S = 1/2$ $[\text{TCNQ}]^-/[\text{TCNE}]^-$, but differing magnetic behaviors. Comparison of the structures and nearest neighbor spin couplings for **MM_{LT}** ($T_c = 2.5$ K), **FO** ($T_c = 3.1$ K), and ferromagnetic $[\text{FeCp}^*_2][\text{TCNE}]$ ($T_c = 4.8$ K), albeit having an even shorter (17.8%) N \cdots N separation with respect to **FO**, has significantly enhanced intrachain ferromagnetic coupling that is accord with the 55% greater T_c for $[\text{FeCp}^*_2][\text{TCNE}]$ with respect to **FO**. This is attributed to the smaller size and concomitant greater spin density for $[\text{TCNE}]^-$ with respect to $[\text{TCNQ}]^-$ providing an enhanced ferromagnetic coupling and a higher T_c that cannot be accounted for from the slightly reduced (3%) intrachain separation.

$[\text{FeCp}^*_2][\text{TCNE}]$, in contrast, only forms one polymorph at room temperature, however, upon cooling two additional phases reversibly form at 280 and 245 K, Scheme 1.^{10,27} Furthermore, solvated pseudo polymorphs of $[\text{FeCp}^*_2][\text{TCNE}]$ have been reported,¹¹ which have yet to be reported for $[\text{FeCp}^*_2][\text{TCNQ}]$. Based upon Kitaigorodskii's principle³⁴ that the more stable polymorph has the higher density,³⁵ based on the room temperature structure, Table 1, **P** is the more stable than the **MM_{RT}** and **FO** polymorphs. This is in accord with **P** also having extra stabilization arising from the intradimer π - $[\text{TCNQ}]_2^{2-}$ multicenter bonding,^{36,37} in addition to the van der Waals interactions that are also present for **MM_{RT}** and **FO**.



Scheme 1. Formation of the five (3 room temperature) forms of $[\text{FeCp}^*_2][\text{TCNQ}]$ (top) and three (1 room temperature) forms of $[\text{FeCp}^*_2][\text{TCNE}]$ (bottom).

A computational nearest-neighbor magnetic coupling analysis based upon the low temperature ($18 \pm 1\text{ K}$) structures suggest dominating intrachain $[\text{FeCp}^*_2]^+ \cdots [\text{TCNQ}]^-$ ferromagnetic spin couplings (4.95 and 6.5 cm^{-1} for **FO** and **MM_{LT}**, respectively) as a consequence of their spins ($S = 1/2$) residing in orthogonal orbitals. All of the nearest neighbor magnetic interactions are ferromagnetic ($J_{ij} > 0$) for the **FO** polymorph in accord with the observed ferromagnetically ordered ground state. Similar results were reported for ferromagnetic

[FeCp*₂][TCNE].¹⁰ Nonetheless, computational results indicate that in contrast to the **FO** polymorph, due to an orientational change and the shortest separation between nearest neighbor [TCNQ]^{•••}[TCNQ][•] antiferromagnetic coupling is calculated for this interaction for the **MM_{LT}** polymorph that is consistent with its antiferromagnetic ground state. Thus, the magnetic ground state cannot be described from the dominant magnetic interactions. Furthermore, the **MM_{RT}** room temperature structure reversibly transforms to the **MM** structure at 226.5 K (-46.7 °C) with an enthalpy of transformation of 0.68 kJ/mol. At 70 ± 10 K, the **MM** structure reversibly transforms to the **MM_{LT}** structure that exhibits metamagnetic behavior. Hence, **MM_{RT}**, **MM**, and **MM_{LT}** result from displacive phase transitions, while **MM**, **P**, and **FO** do not.

Acknowledgment. The authors thank Dr. Joshua D. Bagnato for initial synthesis of metamagnetic [FeCp*₂][TCNQ]. JSM and JGD designed several experiments, synthesized the materials, and determined the spectroscopic, thermal, and magnetic properties, and acknowledge the support provided by the U.S. Department of Energy Grant #DE FG02-93ER45504. SHL and PWS collected and refined the synchrotron powder X-Ray diffraction data at the National Synchrotron Light Source beamline X16C at Brookhaven National Laboratory and acknowledge support by the U.S. Department of Energy, Office of Basic Energy Sciences, under Contract No. DE-AC02-98CH10886. ALR collected and refined the single crystal X-Ray diffraction data. All authors contributed to the writing of the manuscript. MF, JR-A, and JJN provided the computational studies, and thank MINECO for funding (grants MAT2011-25972 and CTQ2017-87773-P using Feder funds) and the Catalan Autonomous Government (grants 2014SGR1422 and 2017SGR348) for funding. M.F. and J.J.N. also thank the allocation of computer time provided by CESCO and BSC. Images of structures were generated using Mercury (CCDC) and CrystalMaker[®]; CrystalMaker Software Ltd, Oxford, England.

Supporting Material

The CCDC deposition numbers for **FO**, **MM** at 17 (**MM_{LT}**), 230, and 295 (**MM_{RT}**) K, are 2069077, 2069078, 2069829, and 2069080, respectively. These data can be obtained free of charge from The Cambridge Crystallographic Data Centre via www.ccdc.cam.ac.uk/data_request/cif.

References

† Stony Brook University

¶ Current Address: Argonne National Laboratory

University of Barcelona

§ University of Utah

‡ University of California, San Diego

(1) Miller, J. S. *Adv. Mater.* **1990**, *2*, 98.

(2) S. J. Blundell, F. L. Pratt *J. Phys.: Condens. Matter*, **2004**, *16*, R771.

V. I. Ovcharenko, R. Z. Sagdeev, *Russ. Chem. Rev.*, **1999**, *68*, 345.

M. Kinoshita, *Phil. Trans. R. Soc. Lond. (A)*, **1999**, *357*, 2855.

J. S. Miller, A. J. Epstein, *Chem. Commun.* **1998**, 1319.

J. S. Miller, A. J. Epstein, *Angew. Chem. Int. Ed. Engl.*, **1994**, *33*, 385.

J. S. Miller, *Chem. Soc. Rev.* **2011**, *40*, 3266.

Thorarinsdottir, A. E.; Harris, T. D. *Chem. Rev.* **2020**, *120*, 8716.

(3) J. M. Williams, J. R. Ferraro, R. J. Thorn, K. D. Carlson, U. Geiser, H. H. Wang, A. M. Kini, M. H. Wangbo, in *Organic Superconductors. Synthesis, Structure, Properties and Theory* (Ed.: R. N. Grimes), Prentice Hall, Englewood Cliffs, New Jersey, USA, 1992

(4) T. Hang, W. Zhang, H.-Y. Ye, R.-G. Xiong, *Chem. Soc. Rev.* **2011**, *40*, 3577.

(5) G. A. Candela, L. J. Swartzendruber, J. S. Miller, M. J. Rice, *J. Am. Chem. Soc.* **1979**, *101*, 2755.

(6) J. S. Miller, J. H. Zhang, W. M. Reiff, L. D. Preston, A. H. Reis, E. Gerbert, M. Extine, J. Troup, M. D. Ward, *J. Phys. Chem.* **1987**, *91*, 4344.

(7) M. L. Taliaferro, F. Palacio, J. S. Miller, *J. Mater. Chem.* **2006**, *16*, 2677.

(8) J. S. Miller, A. J. Epstein, W. M. Reiff, *Mol. Cryst., Liq. Cryst.*, **1985**, *120*, 27.

(9) J. S. Miller, *Adv. Mater.* **2002**, *14*, 1105.

(10) J.-H. Her, P. W. Stephens, J. Ribas-Ariño, J. J. Novoa, W. W. Shum, J. S. Miller, *Inorg. Chem.* **2009**, *48*, 3296.

(11) J. S. Miller, P. K. Gantzel, A. L. Rheingold, M. L. Taliaferro, *Inorg. Chem.* **2009**, *48*, 4201.

(12) J. S. Miller, J. C. Calabrese, H. Rommelmann, S. Chittipeddi, A. J. Epstein, J. H. Zhang, W. M. Reiff, *J. Am. Chem. Soc.* **1987**, *109*, 769.

-
- Miller, J. S.; Calabrese, J. C.; Epstein, A. J.; Bigelow, R. W.; Zhang, J. H.; Reiff, W. M. *J. Chem. Soc. Chem. Commun.* **1986**, 1026
- (13) S. Chittipeddi, K. R. Cromack, J. S. Miller, A. J. Epstein, *Phys. Rev. Lett.*, **1987**, 58, 2695.
- (14) A. H. Reis, L. D. Preston, J. M. Williams, S. W. Peterson, J. S. Miller, *J. Am. Chem. Soc.* **1979**, 101, 2756.
- (15) W. E. Broderick, D. M. Eichhorn, X. Liu, P. J. Toscano, S. M. Owens, B. M. Hoffman, *J. Am. Chem. Soc.* **1995**, 117, 3641.
- (16) J. S. Miller, A. H. Reis, Jr., E. Gerbert, J. J. Ritsko, W. R. Saleneck, L. Kovnat, T. W. Cape, R. P. Van Duyne, *J. Am. Chem. Soc.* **1979**, 101, 7111.
- (17) J. Bernstein, Polymorphism in Molecular Crystals, 2nd ed., Oxford University Press, 2020.
- (18) J. S. Miller, *Adv. Mater.* **1998**, 10, 1553.
- (19) J. S. Miller, A. J. Epstein, *J. Am. Chem. Soc.* **1987**, 109, 3850.
- (20) M. Deumal, M. J. Bearpark, J. J. Novoa, M. A. Robb, *J. Phys. Chem. A* **2002**, 106, 1299.
- (21) A. A. Coelho, TOPAS-Academic, Version 6 Technical Reference.
<http://www.bruker-axs.de>. TOPAS-Academic is available at www.topas-academic.net
- (22) A. A. Coelho, *J. Appl. Cryst.* **2000**, 33, 899.
- (23) A. A. Coelho, *J. Appl. Cryst.* **2003**, 36, 86.
- (24) (a) Saint Plus, v. 6.02; Bruker Analytical X-ray: Madison, WI 1999. (b) G. M. Sheldrick SADABS; University of Göttingen: Göttingen, Germany, 1996.
- (25) G. M. Sheldrick *SHELXL97*, program for the crystal structure refinement, University of Göttingen, Germany, 1997
- (26) N. Augart, R. Boese, G. Schmid, *Z. Anorg. Allg. Chem.* **1991**, 595, 27.
- (27) M. Nakano, M. Sorai, *Mol. Cryst. Liq. Cryst.* **1993**, 233, 161.
- (28) P.-A. Malmqvist, A. Rendell, B. O. Roos, *J. Phys. Chem.* **1990**, 94, 5477.
- (29) MOLCAS: F. Aquilante, L. De Vico, N. Ferré, G. Ghigo, P.-A. Malmqvist, P. Neogady, T. B. Pedersen, M. Pitonak, M. Reiher, B. O. Roos, L. Serrano-Andrés, M. Urban, V. Veryazov, R. Lindh, *J. Comput. Chem.* **2010**, 31, 224.
- (30) The restricted active space is defined as the number of electrons in all RAS space, maximum number of holes in RAS1, maximum number of particles in RAS3; orbitals in RAS1, orbitals in RAS2, orbitals in RAS3 (see Figure S9 for further information)

-
- (31) B. O. Roos, R. Lindh, P.-A. Malmqvist, V. Veryazov, P.-O. Widmark, *J. Phys. Chem. A*, **2004**, *108*, 2851
- (32) R. Prins, F. Reinders, *J. Am. Chem. Soc.* **1969**, *91*, 4929.
- (33) J. Fulara, K. Filipkowski, J. P. Maier, *J. Phys. Chem. C*. **2017**, *121*, 1069.
- (34) A. I. Kitaigorodskii, Organic Chemical Crystallography, Consultants Bureau, NY, 1961.
- (35) Since the density of **P** exceeds the densities of the **MM_{RT}** and **FO** by more than 1%, this assessment is deemed to be more than 90% reliable; A. Burger, R. Ramburger, *Microchem. Acta* **1979**, II, 273.
- (36) I. Garcia -Yoldi, J. S. Miller, J. J. Novoa, *J. Phys. Chem. A*, **2009**, *113*, 7124.
- (37) F. Mota, J. J. Novoa, J. S. Miller, in *Intermolecular interactions in crystals: Fundamentals of Crystal Engineering*, J. J. Novoa, Ed., RSC Publisher, Ch. 17, 595-613, 2017.